Diffraction of flexural waves by cracks in orthotropic thin plates. Part II: far field analysis

PLEASE CITE THE PUBLISHED VERSION

LICENCE

REPOSITORY RECORD

Thompson, Ian, and I. David Abrahams. 2019. "Diffraction of Flexural Waves by Cracks in Orthotropic Thin Plates. Part II: Far Field Analysis". figshare. https://hdl.handle.net/2134/2614.

Diffraction of flexural waves by cracks in orthotropic thin elastic plates.
Part II: far field analysis

By Ian Thompson†and I. David Abrahams‡

†Department of Mathematical Sciences, Loughborough University,
Loughborough, Leicestershire LE11 3TU, UK
‡Department of Mathematics, University of Manchester,
Oxford Road, Manchester M13 9PL, UK

The scattered field arising from diffraction of a plane flexural wave by a semi-infinite crack in an orthotropic Kirchhoff thin plate is analysed. The crack is aligned with a principal direction of the material, so that two of the plate's three planes of symmetry are preserved. An asymptotic approximation is derived via the method of steepest descents, and explicit expressions are given for the most significant contributions. The effects of anisotropy upon the scattered field are made clear, and numerical results are presented for typical engineering materials.

1. Introduction

In a recent article (Thompson & Abrahams, 2005) henceforth referred to as **I**, the authors investigated the scattering of plane flexural waves by a semi-infinite crack in an orthotropic Kirchhoff thin plate. The crack is aligned with a principal direction of the material, and the scattered field is composed of symmetric and antisymmetric components, each of which is expressed in the form of a diffraction integral (Crighton et al., 1992). The present work is concerned with analysis of the aforementioned integrals in the far field, where the observer is located many wavelengths from the crack tip. The method of steepest descents (Jeffreys & Jeffreys, 1956) is employed to obtain the leading order approximation. This arises from a single saddle point and two poles; novel arguments are used to show that branch point contributions are exponentially small. Particular attention is paid to the effects of anisotropy upon the scattered field, several of which are related to the direction of propagation of incident group velocity, which generally differs from that of the phase velocity in an orthotropic medium (Lighthill, 2002). A major mathematical difficulty introduced by anisotropy is that determination of the saddle point's location for a given angle of observation requires the solution of a cubic equation. This is overcome by the introduction of a new parameter, related to the group velocity of the incident wave, in terms of which the saddle point contribution is expressed explicitly. A uniform approximation, which accurately represents the far-field for all angles of incidence and at all angles of observation except on the crack faces is derived. Numerical results are presented for several typical fibre reinforced materi-
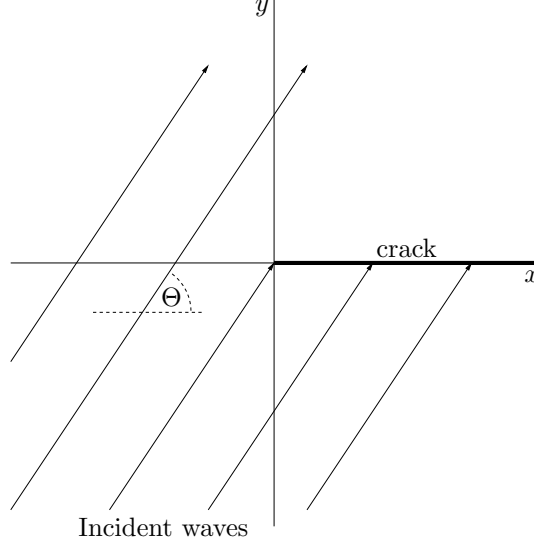
Figure 1. The thin elastic plate with flexural waves incident at angle Θ upon a semi-infinite crack along $x > 0$, $y = 0$.

als, with parameters taken from Kollár & Springer (2003). Corresponding results for the isotropic case have been investigated by Norris & Wang (1994).

The dominant contributions to the scattered response on the crack faces are investigated separately. These are the reflected field (present on the lit side only), and a diffracted *'edge wave'*, which propagates along the faces of the crack and is evanescent in perpendicular directions. Norris (1994) first demonstrated the existence of this type of wave in an orthotropic Kirchhoff plate; the corresponding result for isotropic media is attributed to Konenkov (1960). Thompson et al. (2002) showed that one and only one edge wave propagates along crack faces in orthotropic plates for any angle of inclination between crack and principal axes, and Fu (2003) confirmed this result using a Stroh formalism. Zakharov (2002) has also examined the properties of edge waves on thin anisotropic elastic plates.

2. The boundary value problem and its formal solution

(a) Thin plate equations

Consider an infinite, orthotropic thin plate lying in the (x, y) plane, with a transverse flexural wave W^{inc} incident at angle $\Theta \in [0, \pi)$ upon a semi-infinite, thin crack along the line $y = 0$, $x > 0$; see figure 1. The principal directions of the plate are parallel to the Cartesian axes, and hence transverse motion is governed by the fourth order partial differential equation (Timoshenko & Woinowsky-Krieger, 1959)

$$D_x \frac{\partial^4 W}{\partial x^4} + 2(D_1 + 2D_{xy}) \frac{\partial^4 W}{\partial x^2 \partial y^2} + D_y \frac{\partial^4 W}{\partial y^4} + \rho h \frac{\partial^2 W}{\partial t^2} = 0. \qquad (2.1)$$

The constants ρ and h represent the plate density and thickness respectively, whilst D_x, D_y, D_1 and D_{xy} are parameters that describe the particular material. Since

	E_x (GPa)	E_y (GPa)	G_{xy} (GPa)	ν_{xy} -	ρ (kgm^{-3})	N
Glass/epoxy	38.6	8.27	4.14	0.26	1600	1.579099
Boron/epoxy	204	18.5	5.59	0.23	2000	2.326316
Graphite/epoxy	181	10.3	7.17	0.28	1600	2.387106
Isotropic (epoxy)	3.9	3.9	1.4 (13/9) *	0.35	1270	1.000000

Table 1. *Experimentally measured parameters for typical materials, selected from those given by Kollár & Springer (2003). The first three are composed of an epoxy matrix, with unidirectional fibres parallel to the x axis. The final column shows the normalising factor N (equation 2.16). (*) Note that Kollár & Springer give elastic constants to either two or three significant figures. In order to obtain parameters for a material that is* exactly *isotropic, we have re-calculated the shear modulus in the last case using equations (2.3) and (2.8) to obtain ($G_{xy} = 13/9$).*

the combination occurs frequently, we write

$$H = D_1 + 2D_{xy}, \tag{2.2}$$

as is conventional. A direct physical interpretation of these parameters is difficult, however they are expressed by Norris (1994) in terms of more familiar engineering constants, thus

$$D_x = \frac{h^3}{12}\frac{E_x}{1 - \nu_{xy}\nu_{yx}}, \quad D_y = \frac{h^3}{12}\frac{E_y}{1 - \nu_{xy}\nu_{yx}}, \quad D_1 = \frac{h^3}{12}\frac{\nu_{yx}E_x}{1 - \nu_{xy}\nu_{yx}}, \quad D_{xy} = \frac{h^3}{12}G_{xy}, \tag{2.3}$$

where E_x and E_y are the Young moduli in the x and y directions respectively, and G_{xy} is the shear modulus in the (x, y) plane. The Poisson ratio ν_{xy} is the ratio of extension in the x direction to contraction in the y direction, and vice-versa for ν_{yx}. These are related to the Young moduli via the expression

$$\nu_{yx}E_x = \nu_{xy}E_y. \tag{2.4}$$

Some sample material parameters for typical engineering materials are given in table 1; these will be used throughout this work where numerical examples are required. Now, shear moduli and Young moduli are always strictly positive; therefore it follows immediately that

$$D_x > 0, \qquad D_y > 0, \qquad D_{xy} > 0, \tag{2.5}$$

and in addition, it is possible to establish the inequality

$$D_xD_y > D_1^2, \tag{2.6}$$

via arguments involving strain energy density (Kollár & Springer, 2003). To avoid certain pathological cases, we shall assume that

$$D_1 > -3D_{xy}/2. \tag{2.7}$$

The simplifications arising from this assumption greatly outweigh the slight loss in generality, since materials that violate inequality (2.7) possess negative Poisson

ratios and therefore tend to be unimportant for ordinary engineering applications. Note that (2.7) ensures that $H > 0$. In the particular case of isotropy, we have

$$D_x = D_y = D, \qquad D_1 = \nu D, \qquad D_{xy} = (1 - \nu)D/2, \qquad (2.8)$$

where ν is the Poisson ratio, and D the bending stiffness of the plate.

The incident wave has the form

$$W^{\text{inc}} = \Re\left[e^{i(\mathbf{v}\cdot\mathbf{x})}e^{-i\omega t}\right] \qquad (2.9)$$

where $\mathbf{v}$ is the wavenumber vector, whose elements are

$$v_1 = |\mathbf{v}|\cos\Theta, \qquad\qquad v_2 = |\mathbf{v}|\sin\Theta, \qquad (2.10)$$

ω is the angular frequency of vibrations of the waves, whilst $\mathbf{x}$ simply represents position on the plate, i.e. $\mathbf{x} = (x, y)$. The wavenumber modulus is obtained by substitution of (2.9) into equation (2.1); thus

$$|\mathbf{v}| = \left[\rho h\omega^2/(D_x\cos^4\Theta + 2H\sin^2\Theta\cos^2\Theta + D_y\sin^4\Theta)\right]^{1/4}. \qquad (2.11)$$

The scattered response W, which contains no waves incoming toward $y = 0$, is defined as

$$W = W^{\text{t}} - W^{\text{inc}}, \qquad (2.12)$$

where the superscript 't' refers to the total transverse displacement field. All three terms in equation (2.12) must satisfy (2.1), and the Kirchhoff free edge conditions require that, for $x > 0$,

$$\left[D_1\frac{\partial^2}{\partial x^2} + D_y\frac{\partial^2}{\partial y^2}\right]W^{\text{t}}(x, 0) = 0, \qquad (2.13)$$

and

$$\frac{\partial}{\partial y}\left[(D_1 + 4D_{xy})\frac{\partial^2}{\partial x^2} + D_y\frac{\partial^2}{\partial y^2}\right]W^{\text{t}}(x, 0) = 0. \qquad (2.14)$$

Close to the crack tip, the integrability of strain energy density requires (see **I**) that $W \sim C(\theta)r^\mu$ as $r = \sqrt{x^2 + y^2} \to 0$, where C is some regular function of the variable θ, and $\mu \geq 1$. In general, we work with dimensionless spatial variables $\hat{x}$ and $\hat{y}$, defined so that

$$\hat{x} = \left(\rho^{\text{iso}}h\omega^2/D_x^{\text{iso}}\right)^{1/4}x, \qquad\qquad \hat{y} = \left(\rho^{\text{iso}}h\omega^2/D_x^{\text{iso}}\right)^{1/4}y, \qquad (2.15)$$

where the superscript 'iso' refers to the parameters of the isotropic epoxy plate (table 1). Note that this scaling is conformal; angles in the (x, y) plane are conserved in the $(\hat{x}, \hat{y})$ plane. For equal frequency of excitation, these variables permit comparison of results between different materials of the same thickness. Previously, a material dependent scaling was employed for algebraic convenience, thus in terms of the variables used in paper **I**, we have $(\hat{x}, \hat{y}) = N(x_*, y_*)$, where the normalising factor N is given by

$$N = \left[(\rho^{\text{iso}}D_x)/(\rho D_x^{\text{iso}})\right]^{1/4}. \qquad (2.16)$$

Normalising factors for the materials under consideration in this article are shown in table 1. Note that N is generally larger for materials reinforced by stiffer fibres.
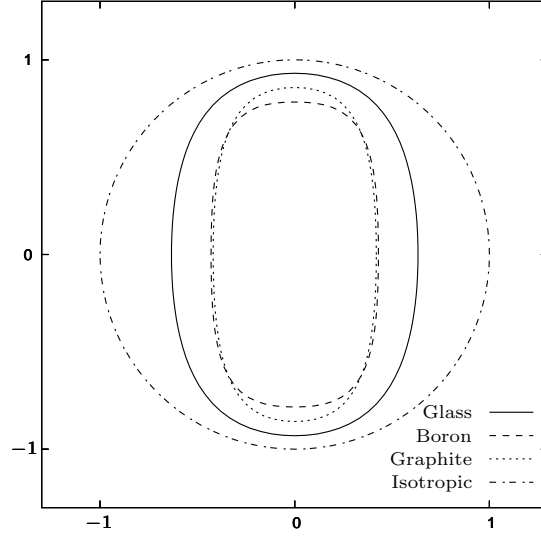
Figure 2. Polar plots of the normalised wavenumber $|\hat{\mathbf{v}}|$ against the direction of phase velocity Θ, for several materials (see table 1). These are equivalent to slowness surfaces with $\omega = 1$.

(b) Group velocity

An important property of waves in anisotropic media is that the group and phase velocity vectors generally differ in both magnitude and orientation. Here, the phase velocity of the incident field is inclined at angle Θ to the x axis, whilst the group velocity vector $\mathbf{U}$ is obtained by differentiation of the angular frequency with respect to the components of the wavenumber vector (Lighthill, 2002). In the two-dimensional case under consideration here, we have

$$\mathbf{U} = (\partial\omega/\partial v_1, \partial\omega/\partial v_2),$$

with

$$\omega = \frac{1}{\sqrt{\rho h}}\sqrt{D_x v_1^4 + 2H v_1^2 v_2^2 + D_y v_2^4}.$$

Making use of equation (2.10) now yields

$$\mathbf{U} = 2|\mathbf{v}|^3(\rho h\omega)^{-1}\Big([D_x\cos^2\Theta + H\sin^2\Theta]\cos\Theta, [D_y\sin^2\Theta + H\cos^2\Theta]\sin\Theta\Big).$$

Thus, the angle of inclination of U to the x axis is Ψ, where

$$\Psi(\Theta) = \arctan[Q(\Theta)\tan\Theta] \quad (\in [0,\pi]), \tag{2.17}$$

and

$$Q(\Theta) = (H\cos^2\Theta + D_y\sin^2\Theta)/(H\sin^2\Theta + D_x\cos^2\Theta). \tag{2.18}$$

Note that

$$\Psi(\pi - \Theta) = -\Psi(\Theta). \tag{2.19}$$

In general, $\Theta \neq \Psi$, though they coincide when $\Theta \in \{0, \frac{\pi}{2}, \pi\}$. In an isotropic material, the two are identical, as we should expect. To illustrate the differing orientation of phase and group velocity, a polar plot known as a slowness surface is usually employed. These have argument Θ, and their magnitude is the reciprocal of the wavespeed, i.e. $1/c = |\mathbf{v}|/\omega$. The outgoing normal to the plot gives the direction of propagation of group velocity. Since the frequency ω is unspecified, figure 2 shows 'shortness surfaces', for the materials given in table 1. The magnitude of these is the reciprocal of normalised wavelength, i.e.

$$\omega/\hat{c} = |\hat{\mathbf{v}}|;$$

they are equivalent to slowness surfaces with $\omega = 1$. Note that neither frequency, nor the choice of conformal scaling affects the shape of the surface, merely its magnitude. The three composite materials have unidirectional fibres parallel to the x axis, so $D_x \gg D_y$, i.e. their stiffness is much greater in the x direction than in the y direction. The wavelength increases with the stiffness of the material, hence under equal frequency of excitation, the plane wave travels with greater phase velocity in a more rigid medium. Consequently, in the fibre composites, the waves propagate most rapidly in the x direction. The shape of the polar plots also shows that the group velocity is orientated towards the direction parallel to the fibres. As the phase velocity approaches orthogonality to the fibre direction, the direction of energy propagation changes rapidly, so that the two coincide for $\Theta = \frac{\pi}{2}$ and $\Theta = \frac{3\pi}{2}$.

(c) The formal solution

The solution to the diffraction problem outlined in §2a was solved exactly in **I** by means of the Wiener-Hopf technique. We have

$$W(\hat{x}, \hat{y}) = \frac{1}{2\pi i} \int_{\mathcal{C}} \left(f_1(\alpha) e^{-\lambda_1(\alpha)\hat{y}/N} + f_2(\alpha) e^{-\lambda_2(\alpha)\hat{y}/N} \right) \frac{e^{-i\alpha\hat{x}/N} \, d\alpha}{(\alpha - \alpha_0)\phi(\alpha)\lambda_1(\alpha)}, \tag{2.20}$$

where the location of the specular singularity, which plays a key role in the solution, is given by

$$\alpha_0 = -k(\Theta)\cos\Theta, \tag{2.21}$$

with the function $k(\Theta)$ defined as

$$k(\Theta) = \left[D_x/(D_x \cos^4\Theta + 2H\cos^2\Theta\sin^2\Theta + D_y\sin^4\Theta) \right]^{1/4}; \tag{2.22}$$

this is actually the non-dimensional wavenumber of the incident field under the scaling used in **I**. The path of integration $\mathcal{C}$ traverses the real line for large $|\alpha|$, and is indented above any singularities on the real line in $\alpha \leq \alpha_0$ and below singularities on the real line for which $\alpha > \alpha_0$; see **I** for details. The two functions appearing in the exponents are defined by

$$\lambda_m(\alpha) = \left[H\alpha^2 + (-1)^m D_x\phi \right]^{1/2} \Big/ \sqrt{D_y}, \tag{2.23}$$

in which $m \in \{1, 2\}$, and

$$\phi(\alpha) = \left[(H^2 - D_x D_y)\alpha^4 + D_x D_y \right]^{1/2} \Big/ D_x. \tag{2.24}$$

Note that the surd symbol $\sqrt{\cdot}$ refers to the positive root of a positive real number; this is the only context in which it is used herein. The other elementary functions present in equation (2.20) and are defined via

$$L_m(\alpha) = \left[2D_{xy}\alpha^2 + (-1)^m D_x \phi\right]/D_x, \tag{2.25}$$

and

$$\gamma_-(\alpha) = -\mathrm{i}\sqrt[4]{D_x/D_y}[(\alpha-1)(\alpha-\mathrm{i})]^{1/2}. \tag{2.26}$$

The last function is analytic on and below the contour $\mathcal{C}$, and hence it is given the subscript '$-$' to signify analyticity in this region. It is obtained from a product factorisation of the function $\gamma(\alpha)$, defined as

$$\gamma(\alpha) = \sqrt{D_x/D_y}(\alpha^4-1)^{1/2}. \tag{2.27}$$

Functions that are analytic both on and above $\mathcal{C}$ are denoted by a subscript '$+$'. To complete these definitions, we must specify values of all multifunctions at a point in the α plane; it is useful to choose α_0, which lies in the interval $[-1, 1]$. We denote a function evaluated at this point with a superscript '0'. Thus, we have

$$\phi^0 = k^2(\Theta)\left(H\cos^2\Theta + D_y\sin^2\Theta\right)/D_x, \tag{2.28}$$

which implies that λ_1 (λ_2) has branch points at $\alpha = \pm 1$ $(\alpha = \pm\mathrm{i})$. Furthermore,

$$\lambda_1^0 = -\mathrm{i}k(\Theta)\sin\Theta, \tag{2.29}$$

$$\lambda_2^0 = k(\Theta)\sqrt{2H\cos^2\Theta + D_y\sin^2\Theta}\big/\sqrt{D_y}, \tag{2.30}$$

$$\gamma^0 = -\mathrm{i}k^2(\Theta)\sin\Theta\sqrt{2H\cos^2\Theta + D_y\sin^2\Theta}\big/\sqrt{D_y}, \tag{2.31}$$

and

$$\gamma_-^0 = \sqrt[4]{D_x/D_y}\sqrt{1 + k\cos\Theta}[-k(\Theta)\cos\Theta - \mathrm{i}]^{1/2}, \tag{2.32}$$

where, in the latter case, the fractional power has its argument in the interval $(-\frac{\pi}{2}, \frac{\pi}{2}]$. Finally, equation (2.30) implies that $\Re[\lambda_2] > 0$ for $\alpha \in \mathbb{R}$, thus the function λ_1 may be evaluated for $\alpha \in \mathbb{R}$ by writing $\lambda_1 = \gamma/\lambda_2$.

We also require the function $K(\alpha)$, which is defined via

$$K(\alpha) = 2\phi/(L_1^2\lambda_2 - L_2^2\lambda_1), \tag{2.33}$$

along with its product factorisation, i.e. $K = K_+K_-$ (where '$\pm$' subscripts are defined as above but with the additional property of no zeros in the indicated upper/region), subject to the symmetry relationship $K_+(-\alpha) = K_-(\alpha)$. Full details of the product decomposition are given in **I**; here we need only note that K_+ has simple poles at the points $\alpha = -\alpha_e$ and $\alpha = -\mathrm{i}\alpha_e$, where α_e is the positive real constant

$$\alpha_e = \left\{D_xD_y\Big/\left[D_xD_y - \left(\sqrt{4D_{xy}^2 + D_1^2} - 2D_{xy}\right)^2\right]\right\}^{1/4}, \tag{2.34}$$

and also branch points at $\alpha = -1$ and $\alpha = -\mathrm{i}$. The function ϕ has finite branch cuts on the line sections $[\alpha_\phi, \mathrm{i}\alpha_\phi]$ and $[-\alpha_\phi, -\mathrm{i}\alpha_\phi]$, where

$$\alpha_\phi = \left[D_x D_y / (D_x D_y - H^2) \right]^{1/4}. \tag{2.35}$$

Branch cuts are also positioned along the line segments $\alpha = \pm(1 + \mathrm{i})u$ and $\alpha = \pm\mathrm{i}(1 + u)$, $u \geq 0$, so that λ_1, λ_2, γ_- and K_+ are analytic within the cut plane. Note that these are slightly different from the branch cuts used in **I**; the reconfiguration required here changes certain functions in equation (2.20) within regions through which $\mathcal{C}$ does not pass, and so the solution is unaffected. A side effect of this is that a pole of K_+ may appear in the lower half plane on the line $\Re[\alpha] = \Im[\alpha]$. On deformation of $\mathcal{C}$ by the method of steepest descents, the residue from this pole is found (numerically) to be exponentially small whenever it is present in the solution, and thus it is omitted from subsequent asymptotic analysis.

The solution may now be completed by defining the functions $f_1(\alpha)$ and $f_2(\alpha)$ in the symmetric and anti-symmetric cases. We have

$$f_1^S = \tfrac{1}{2} K_-^0 K_+ L_1^0 L_1 \gamma_-^0 \gamma_+, \qquad f_2^S = -\tfrac{1}{2} K_-^0 K_+ (\lambda_1)^2 L_1^0 L_2 \gamma_-^0 / \gamma_-, \tag{2.36}$$

where $K_\pm^0 = K_\pm(\alpha_0)$, and

$$f_1^A = -\tfrac{1}{2} K_-^0 K_+ \lambda_1^0 \lambda_1 L_2 L_2^0, \qquad f_2^A = \tfrac{1}{2} K_-^0 K_+ \lambda_1^0 \lambda_1 L_2^0 L_1. \tag{2.37}$$

Here, we have omitted the argument α, as we will henceforth when no ambiguity can arise. Immediately, we have

$$f_1^S(\alpha_0)/(\phi^0 \lambda_1^0) = (1 - c)/2, \qquad f_1^A(\alpha_0)/(\phi^0 \lambda_1^0) = (1 + c)/2, \tag{2.38}$$

where c is the reflection coefficient for the free edge, i.e.

$$c = \left. \frac{L_2^2 \lambda_1 + L_1^2 \lambda_2}{L_2^2 \lambda_1 - L_1^2 \lambda_2} \right|_{\alpha = \alpha_0}. \tag{2.39}$$

Note that both γ_- and λ_1 vanish as $\alpha \to 1$, and so therefore does the diffraction integral (2.20) in the limit $\Theta \to \pi$.

3. Analysis of the solution

(a) The steepest descent paths and the branch cut contribution

We now apply the method of steepest descents to the diffraction integral (2.20). Thus, introduce polar co-ordinates $(\hat{r}, \theta)$; $\hat{r} = \sqrt{\hat{x}^2 + \hat{y}^2}$, with the half-line $\theta = 0$ positioned along the crack. We will consider $\theta \in [0, \pi]$, since the solution in the region where $y < 0$ can be constructed by symmetry. Now, write

$$\chi_m(\alpha, \theta) = \lambda_m \sin \theta + \mathrm{i}\alpha \cos \theta, \quad m \in \{1, 2\}. \tag{3.1}$$

Our overall strategy for analysing the behaviour of (2.20) in the far-field $\hat{r} \gg 0$ is as follows. First, note that the integrand is analytic at the points $\alpha = \pm\alpha_\phi$ and $\alpha = \pm\mathrm{i}\alpha_\phi$, since encircling any one of these points effects the transformations

$\phi \to -\phi$, $\lambda_1 \leftrightarrow \lambda_2$, and $L_1 \leftrightarrow L_2$, leaving the overall expression unchanged. Details can be found in **I**. We will show that a single simple saddle, at which $\partial\chi_1/\partial\alpha = 0$, exists in the interval $[-1, 1]$, and denote this point α_s. By considering the behaviour of both χ_1 and χ_2 on the associated steepest descent path $\mathcal{S}$, on which

$$\Im[\chi_1(\alpha, \theta)] = \Im[\chi_1(\alpha_s, \theta)], \qquad \Re[\chi_1(\alpha, \theta)] \geq \Re[\chi_1(\alpha_s, \theta)].$$

it will be established that contributions with exponent χ_2 are asymptotically negligible, except on the crack face $\theta = 0$. This is advantageous, since analyticity at the branch points of the function ϕ is maintained. If terms with differing exponents are separated, the number of branch points in the α plane is increased from four to eight, and it is difficult to establish which, if any, of these contribute significantly to the approximation. This approach is always valid for materials with $H^2 \leq D_x D_y$, and fortunately all of the materials given in Kollár & Springer (2003) and also in Jones (1975) fall into this category. Thompson (2003) briefly discusses the difficulties that can arise in cases where $H^2 > D_x D_y$, though it is not clear what types of material satisfy this condition. Moreover, by diverting $\mathcal{S}$ in an appropriate manner, we will show that contributions from the branch points $\alpha = \pm i$ are also negligible.

The actual location of the saddle point within the interval $[-1, 1]$ is examined in §3b. This is of crucial importance, since, if the position of the observer is such that $\alpha_s > \alpha_0$, we need not include a residue contribution from the specular pole, whereas if $\alpha_s < \alpha_0$, the residue eliminates the incident field in the shadow region above the crack, and activates the reflected field below the crack. The lines on which $\alpha_s = \alpha_0$ are known as the optical boundaries of shadow and reflection, and the their immediate neighbourhoods are the transition, or Fresnel, regions. The contribution from the saddle $\alpha = \alpha_s$ is then determined. This yields a nonuniform approximation, which describes the leading order behaviour of the diffracted field, away from the face of the crack, provided that the observer is not located in either of the Fresnel regions. A uniform asymptotic result, which provides a valid approximation even when the observer is positioned inside an overlap of the two Fresnel regions, is derived in section §3c. The dominant contributions on the crack faces come from the reflected field and the diffracted edge waves; these are examined in sections §3d and §3e, respectively.

Now, from equation (3.1), a saddle point of the function χ_1 occurs when

$$i\lambda_1'(\alpha) = \cot\theta, \tag{3.2}$$

where the prime symbol refers to differentiation with respect to α, as it does henceforth. Note that the right hand side of this equation can take any real value. The first derivative of λ_1 is

$$\lambda_1'(\alpha) = \frac{\alpha}{D_y \lambda_1} \left[H + \frac{\alpha^2(D_x D_y - H^2)}{D_x \phi} \right], \tag{3.3}$$

hence $i\lambda_1' \to \mp\infty$ as $\alpha \to \pm 1$, since λ_1 is negative imaginary for $\alpha \in (-1, 1)$. Thus, by the intermediate value theorem, there is at least one saddle point in this interval. To demonstrate that there is precisely one saddle point for each θ, we note that the second derivative is given by

$$\lambda_1''(\alpha) = -\left[3\alpha^2(D_x D_y - H^2)(D_x \phi - H\alpha^2) + H D_x D_y \right] / [D_x^2 D_y \phi^3 \lambda_1^3]. \tag{3.4}$$

Equating this to zero, we find that

$$-3\alpha^2(D_x D_y - H^2)(D_x\phi - H\alpha^2) = HD_x D_y$$

which is impossible, since the left hand side is non-positive. Consequently, $\mathrm{i}\lambda_1'$ is monotonic on the interval $(-1, 1)$, and the result follows. Additional saddles may occur elsewhere, though these do not interfere with the approximation. In general, the steepest descent paths must be mapped numerically, since an explicit parametrisation is prohibitively difficult to obtain. Note that (3.4) shows that $\chi_1''(\alpha, \theta)$ is negative imaginary for $\alpha \in [-1, 1]$, so that taking $\alpha = \alpha_s$ yields the minimum value for $\Im[\chi_1]$ on this interval, and, in particular, the quantity $\chi_1(\alpha_0, \theta) - \chi_1(\alpha_s, \theta)$ is always positive imaginary.

There are now two issues to consider, namely the orientation of the path with respect to the branch points at $\alpha = \pm \mathrm{i}$, and the behaviour of the secondary exponent χ_2 on the same descent path as for χ_1. We need only consider $\theta \in (0, \frac{\pi}{2}]$, since the transformation $\alpha \to -\alpha$ gives the steepest descent path for $\pi - \theta$. In this domain, the paths lie in the lower half plane for the most part, as we shall see, and we must determine the nature of the branch cut contribution on the negative imaginary axis. It is instructive to briefly consider the isotropic case, in which the descent paths are given by

$$\alpha^2 + 2\cos\theta(1 + \mathrm{i}u)\alpha - u^2 + 2u\mathrm{i} + \cos^2\theta = 0. \tag{3.5}$$

Here, $u \geq 0$ and the different branches refer to the two parts of the steepest descent contour emanating from the saddle point. Taking real and imaginary parts, it is easy to show that the imaginary axis is crossed at the point $\alpha = -\mathrm{i}\cot\theta$. Thus, the path must be diverted if $\theta < \frac{\pi}{4}$, passing up the left side of the cut to the branch point $\alpha = -\mathrm{i}$, and down the right face. The functions λ_1 and λ_2 are pure imaginary on the diverted section of the path, so the dominant contribution comes from the branch point, where we have

$$\Re[\chi_1] = \Re[\chi_2] = \cos\theta \quad (> 1/\sqrt{2}).$$

In this case, therefore, the branch cut contribution is easily seen to be exponentially small. Now, the functions λ_1 and λ_2 generally possess non-zero real parts on the line segment $(-\mathrm{i}\alpha_\phi, -\mathrm{i}\infty)$. Thus, in anisotropic cases, the path cannot be diverted along the faces of the branch cut, since this may cause exponential growth. To overcome this problem, and establish that the branch cut contribution is exponentially small, we divert the path of integration in such a way that the functions λ_m are prevented from entering the left half plane. The diversion takes place in the lower half plane and so we have $\Re[\chi_m] > |\Im[\alpha]|\cos\theta$. Thus, we seek the lines on which $\Re[\lambda_m] = 0$, to obtain

$$\alpha^2 = -Hu^2/\sqrt{D_x D_y - H^2} \pm (1 - u^4)^{1/2}, \tag{3.6}$$

where $u \geq 0$. By taking into account the various roots, $u \leq 1$ gives possible values for α on the line intervals $[-1, 1]$ and $[-\mathrm{i}\alpha_\phi, \mathrm{i}\alpha_\phi]$, whilst $u \geq 1$ represents two curves that are symmetric about the imaginary axis. That which lies in the lower half plane crosses the imaginary axis at the point $-\mathrm{i}\alpha_d$, where

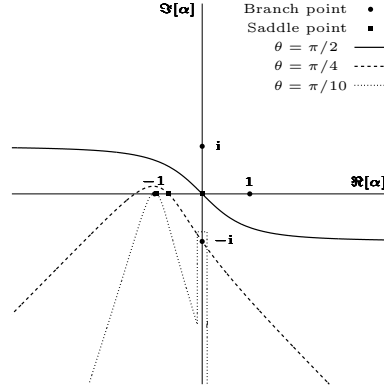$$\alpha_d = \sqrt[4]{H^2/(D_x D_y - H^2)};$$

Figure 3. Steepest descent paths in the isotropic case. For $\theta \geq \pi/4$ the contour has the correct orientation with respect to all of the branch points, whereas if $\theta < \pi/4$, it must be diverted as shown. The contribution from the branch point is exponentially small.

note that $|\alpha_d| < |\alpha_\phi|$. We construct a contour which consists of this curve, and in cases where $|\alpha_d| > 1$, the two faces of the branch cut on the line section $[-i\alpha_d, -i]$. If the steepest descent path passes below the branch point, then it must strike this contour, and at this point, we leave the former and follow the diversion in the appropriate direction. Subsequently, we have $\Re[\lambda_1] = 0$, and $\Re[\lambda_2] \geq 0$, this inequality being strict on the curved section, since $\Re[\lambda_1] = \Re[\lambda_2] = 0$ implies that $\Im[\gamma] = 0$ which can occur only on the axes. The largest contribution from this diversion comes from the point at which the imaginary axis is crossed, where

$$\Re[\chi_2] \geq \Re[\chi_1] = \min\{|\alpha_d|, 1\} \cos\theta.$$

Figure 3 shows steepest descent paths for the isotropic case at angles of incidence $\theta = \pi/2$, $\pi/4$ and $\pi/10$. In the latter case, a diversion around the branch point at $\alpha = -i$ is required.

Having dealt with the branch point, we now examine the behaviour of the secondary exponent on the deformed integration path. Note that at the saddle point, we have $\Re[\chi_2] > \Re[\chi_1]$, and at any point where equality should occur

$$\lambda_1 - \lambda_2 = \sqrt{2}iu,$$

for some $u \in \mathbb{R}$. Solving this equation for α^2, we find that

$$\alpha^2 = \left\{-HD_yu^2 \pm \left[D_xD_y(D_y^2u^4 + D_xD_y - H^2)\right]^{1/2}\right\}/(H^2 - D_xD_y),$$

which can occur only on the real and imaginary axes. On the imaginary axis, $\Re[\chi_2] > \Re[\chi_1]$ for $|\alpha| < 1$, the only region in which this line may be crossed. Similarly, on the real axis, we can only have $\Re[\chi_1] = \Re[\chi_2]$ if ϕ is pure imaginary, i.e. $|\alpha| > \alpha_\phi$. Thus, consider the path to the left of the saddle. On the section in the upper half plane, χ_1 is on its steepest descent path, and $\Re[\chi_2] > \Re[\chi_1]$. If the line section $(-\infty, -\alpha_\phi)$ is crossed, then we subsequently have $\Re[\chi_1] > \Re[\chi_2]$, however following this λ_1, λ_2, and $i\alpha$ all lie in the right half plane, and there is no possibility of exponential growth. Note that it may be necessary to follow the curve on which
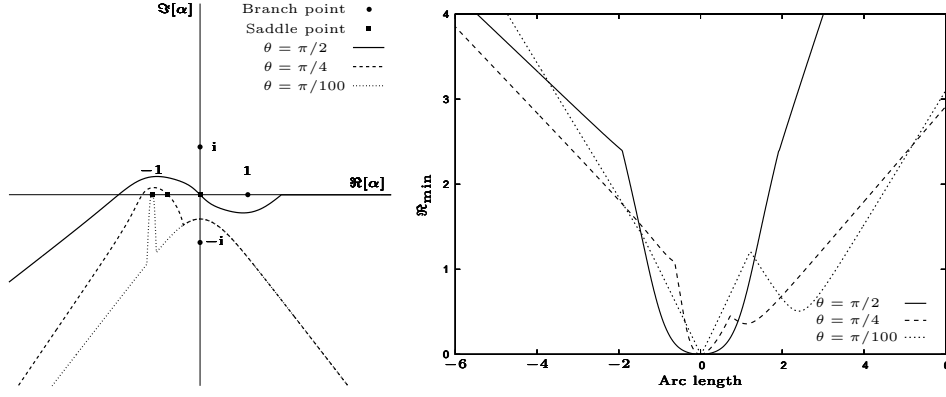
Figure 4. Left: the deformed integration paths for a boron/epoxy composite plate with observation angles $\theta = \frac{\pi}{2}$, $\theta = \frac{\pi}{4}$ and $\theta = \frac{\pi}{100}$. In the case $\theta = \frac{\pi}{100}$, the saddle is very close to the branch point $\alpha = -1$. Right: the smaller real part $\Re_{\min}$ of the two exponent functions χ_1, χ_2 evaluated on the deformed integration path. Positive (negative) arc length refers to the branch of the path to the right (left) of the saddle. Note that discontinuities in the gradient of $\Re_{\min}$ can occur at points where the integration path is diverted, and also where $\Re[\chi_1] = \Re[\chi_2]$.

$\Re[\lambda_1] = 0$ into the lower left quadrant if an intersection with the steepest descent path should occur in the region $\Re[\alpha] < -1$, see for example $\theta = \frac{\pi}{100}$ in figure 4. A similar argument applies to the right of the saddle, however if the line section (α_ϕ, ∞) is crossed, then $i\alpha$ moves into the left half plane, and we shall subsequently have $\Re[\chi_1] > \Re[\chi_2]$. To ensure that this does not cause exponential growth, we divert the path to run to the right along the real axis, rather than allow it to cross into the upper half plane.

Figure 4 shows the deformed integration contours for the boron/epoxy composite (table 1) at observation angles $\theta = \frac{\pi}{2}$, $\theta = \frac{\pi}{4}$ and $\theta = \frac{\pi}{100}$. Also shown are the values of $\Re_{\min} = \min\{\Re[\chi_1], \Re[\chi_2]\}$ on the integration path. The real parts of the exponent functions decline as the diversion path climbs toward the imaginary axis crossing point, however they remain much greater than $\Re[\chi_1(\alpha_s, \theta)]$, which is always zero. Overall, therefore, the dominant contribution comes from the saddle point, $\alpha = \alpha_s$. The terms with exponent function χ_2 are, in general, exponentially small here, except on the crack faces. The evanescent wave pole, $\alpha = -i\alpha_e$ always remains in the region of the plane beneath the integration path, and is therefore unimportant. Note that in the isotropic case, the branch points of the function ϕ disappear to infinity, so in this limit the diversion procedure reduces to following the faces of the branch cut, as above.

(b) The saddle point and the diffraction coefficient

The actual location of the saddle point α_s is difficult to express in terms of θ, generally requiring the solution of a cubic equation. To overcome this problem, we introduce a new parameter β, defined so that

$$\alpha_s = -k(\beta)\cos\beta, \tag{3.7}$$

where $k(\beta)$ is obtained from equation (2.22). Now β and θ both equal zero if $\alpha_s = -1$ and π when $\alpha_s = 1$. The two also coincide at $\frac{\pi}{2}$ when $\alpha_s = 0$, and they are identical in the special case of isotropy. By varying β from 0 to π, we will span the entire range of possible values for α_s; in fact there is a one-to-one correspondence between these variables, as proven by differentiating (3.7) with respect to β—the result is non-zero for $\beta \in (0, \pi)$. In terms of β, we can obtain useful, closed form expressions for quantities that would otherwise be implicit. Indeed, evaluations of several important functions at the saddle point can be obtained immediately from (2.28–2.32) by replacing Θ with β. If the value of β is required for a specific θ, then the cubic equation

$$D_y \tan^3 \beta - H \tan \theta \tan^2 \beta + H \tan \beta - D_x \tan \theta = 0$$

must be solved, however θ is easily expressed in terms of β, since we have

$$\chi_1'[-k(\beta) \cos \beta, \theta] = 0.$$

Making use of (3.3), we find that

$$\theta = \arctan \left[Q(\beta) \tan \beta \right], \tag{3.8}$$

wherein $Q(\beta)$ is defined by equation (2.18). This also leads directly to the relations

$$\cos \theta = \frac{\cos \beta}{\sqrt{\cos^2 \beta + Q^2(\beta) \sin^2 \beta}}, \quad \sin \theta = \frac{Q(\beta) \sin \beta}{\sqrt{\cos^2 \beta + Q^2(\beta) \sin^2 \beta}}; \tag{3.9}$$

note in the former case that $\mathrm{sgn}(\cos \theta) = \mathrm{sgn}(\cos \beta)$.

Equation (3.8) brings to light a key effect of anisotropy: the saddle point and specular pole coalesce when $\beta = \Theta$, and not in general at $\theta = \Theta$, so that the region where $\beta < \Theta$ is in shadow. In terms of the actual angle of observation, $\theta = \Psi$ gives the location of the shadow boundary, where Ψ is the angle of inclination of the incident wave group velocity to the x-axis (see equation 2.17). Thus, the shadow boundary represents the distinction between the presence and absence of energy from the incident field. The precise effect of this varies, depending upon the material parameters, and angle of incidence. For the fibre reinforced composites examined here (see table 1), we have $D_x \gg D_y \approx H$, therefore for small incidence angles, we have $Q(\Theta) < 1$, and hence $\Psi < \Theta$, i.e. the anisotropy causes the shadow region to contract in this case. The opposite is true if $\Theta > \frac{\pi}{2}$ when the shadow region is expanded; both of these effects are due to the tendency of the group velocity to propagate in the fibre direction. If $\Theta \approx \frac{\pi}{2}$, then we have $Q(\Theta) \approx 1$, and consequently $\Psi \approx \Theta$. This behaviour is evident from figure 5, which shows Ψ as a function of incidence angle, with $\Theta \in [0, \frac{\pi}{2}]$. Values of Ψ for $\Theta > \frac{\pi}{2}$ may be inferred from equation (2.19). Obviously, for the isotropic material, the plot is simply the straight line $\Theta = \Psi$. Figure 5 also shows the location of the saddle point as a function of observation angle. As above, we need only consider $\theta \in [0, \frac{\pi}{2}]$, since $\alpha_s(\pi - \theta) = -\alpha_s(\theta)$. The differing gradients can affect the width of the Fresnel regions; this is particularly noticeable for $\theta \approx \frac{\pi}{2}$ in the case of the boron/epoxy composite, where the variation of α_s with θ is very rapid.
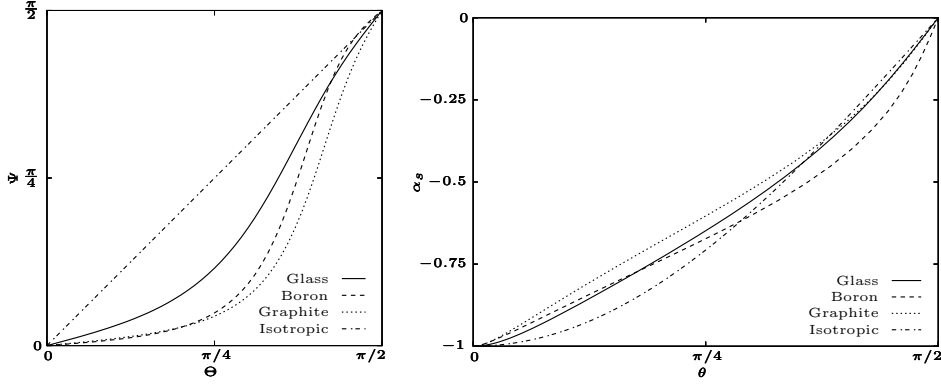
Figure 5. Left: Direction of propagation of group velocity, Ψ as a function of incidence angle Θ. Right: Location of the saddle point α_s as a function of observation angle θ.

A crude, but nevertheless useful approximation to the saddle point contribution can now be obtained by assuming that α_s is not close to α_0 and using the standard steepest descent formula (Jeffreys & Jeffreys, 1956); thus

$$W^{\mathrm{sad}}(\hat{r},\theta) \sim \frac{-\mathrm{e}^{\mathrm{i}\frac{\pi}{4}} D(\theta)}{\sqrt{\hat{r}/N}} \mathrm{e}^{-\hat{r}\chi_1(\alpha_s,\theta)/N} \tag{3.10}$$

where the diffraction coefficient $D(\theta)$ is given by

$$D(\theta) = \frac{f_1(\alpha_s)}{\sqrt{2\pi}} \left[(\alpha_s - \alpha_0)\phi(\alpha_s)\lambda_1(\alpha_s)\sqrt{|\chi_1''(\alpha_s,\theta)|} \right]^{-1}. \tag{3.11}$$

Evaluating the exponent function χ_1 at the saddle point in terms of β, we obtain

$$\begin{aligned} \chi_1(\alpha_s,\theta) &= -\mathrm{i}k(\beta)\cos(\beta - \theta) \\ &= -\frac{\mathrm{i}D_x}{k^3(\beta)} \left[(D_x\cos^2\beta + H\sin^2\beta)^2\cos^2\beta + (D_y\sin^2\beta + H\cos^2\beta)^2\sin^2\beta \right]^{-1/2}. \end{aligned} \tag{3.12}$$

Thus in anisotropic cases, the diffracted field possesses a θ (or β) dependent exponent, whereas for an isotropic material, this expression simplifies to $-\mathrm{i}$, for all θ. Hence, the exponential factor in the diffracted field in an orthotropic material oscillates as θ is varied, in contrast to the special case of isotropy. The frequency of these oscillations increases with $\hat{r}$. Figure 6 shows plots of $\Im[\chi_1^s]/N$, against θ, where N is given by equation (2.16). Here, steep gradients represent rapid oscillation. Each curve is symmetric about $\frac{\pi}{2}$; this is easily seen from equations (3.8) and (3.12), or alternatively by noting that replacing θ with $\pi - \theta$ changes α_s to $-\alpha_s$. The most rapid oscillations occur in the graphite/epoxy composite, at observation angles in the intervals $[0, \frac{\pi}{4}]$ and $[\frac{3\pi}{4}, \pi]$. Note that the oscillations almost cease in the vicinity of $\theta = \frac{\pi}{2}$.
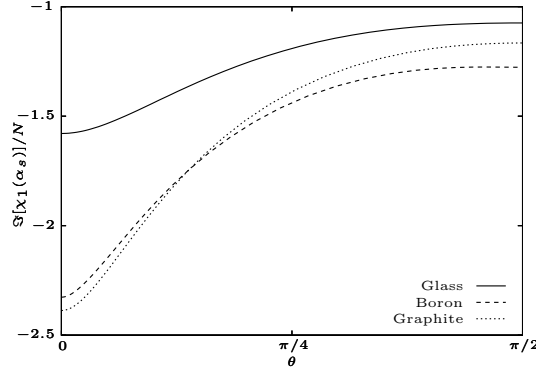
Figure 6. Variation of the exponential term in the saddle contribution with observation angle θ.

Some simplifications in the expression for $D(\theta)$ are available. In particular, we have

$$\frac{1}{\phi(\alpha_s)\lambda_1(\alpha_s)\sqrt{|\chi_1''(\alpha_s,\theta)|}} =$$

$$\mathrm{i}\left[\frac{D_x}{k(\beta)Q(\beta)}\frac{(H\cos^2\beta + D_y\sin^2\beta)\sqrt{\cos^2\beta + Q^2(\beta)\sin^2\beta}}{(3D_xD_y - H^2)\cos^2\beta\sin^2\beta + H(D_x\cos^4\beta + D_y\sin^4\beta)}\right]^{1/2} ; \quad (3.13)$$

note that the quantity in square brackets is positive real and bounded for all $\beta \in [0,\pi]$.

In general, the oscillatory behaviour of the diffracted field, and the build-up of its strength close to the optical boundaries are the dominant effects present, though there are others. To distinguish these, we define a non-specular diffraction coefficient, which is given by

$$\hat{D}(\theta) = \sqrt{N}(\alpha_s - \alpha_0)D(\theta). \quad (3.14)$$

Here, the factor $\sqrt{N}$ is included so that results for different materials are comparable. Figure 7 shows polar plots, with radius $|\hat{D}|$ and argument θ, for various values of the incidence angle Θ. The process of taking moduli in obtaining $|\hat{D}|$ leads to plots which are largely, though not entirely, symmetric. The isotropic material, which has the lowest stiffnesses has the weakest diffracted field. This is to be expected, since the smaller values of N imply that decaying modes travel further in stiffer materials. In general, $\hat{D}$ increases with Θ, though for large incidence angles it decays, finally disappearing as $\Theta \to \pi$. In terms of the observation angle, θ, the field is strongest near to the crack, and weakest for $\theta = \pi$. For the orthotropic materials, the tendency of the energy to propagate in the principal directions causes the maximum to be particularly strong.

(c) The uniform approximation

Now, the approximation given by (3.10) is nonuniform in the sense that it is singular on the optical boundary where $\beta = \Theta$. A uniform asymptotic representation
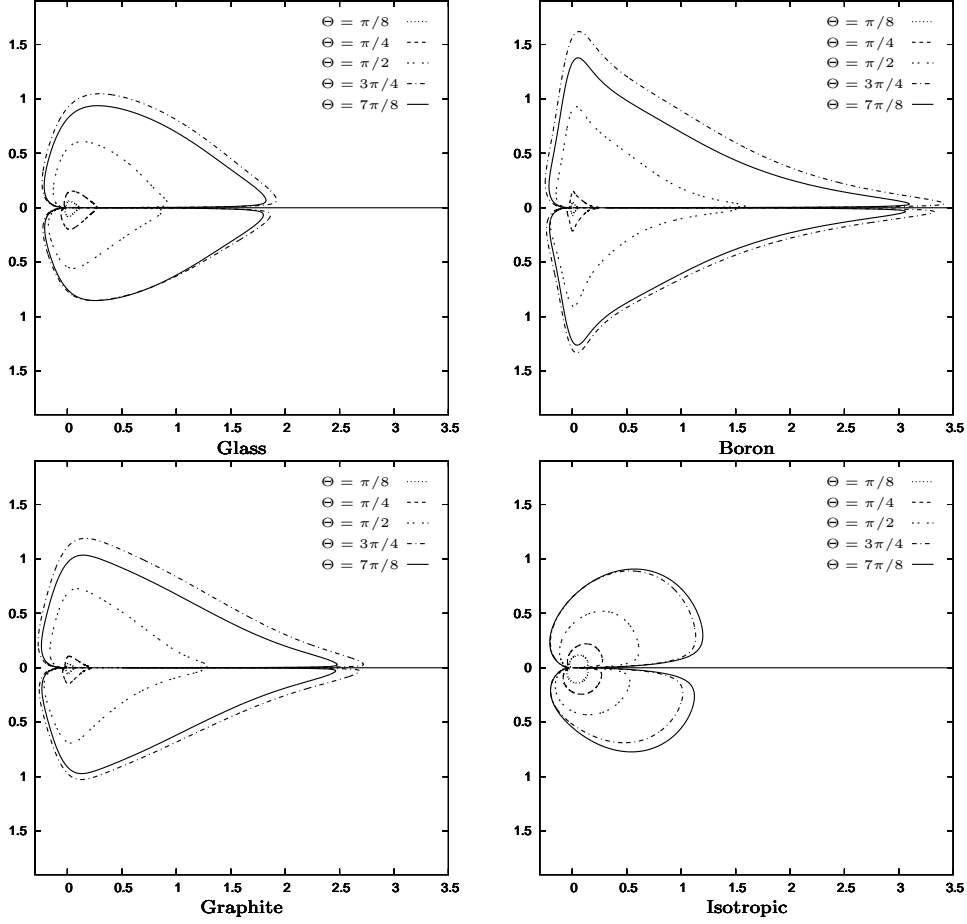
replacemen

Figure 7. Polar plots of the modulus of $\hat{D}(\theta)$, the non-specular diffraction coefficient.

for W can be obtained, which takes into account the effect of the specular pole $\alpha = \alpha_0$, by including a correction term which rapidly but continuously activates the residue from the pole as the optical boundary is crossed. Since the steepest descent path always has the correct orientation with respect to the branch points $\alpha = \pm 1$, these do not contribute directly, however they do have a more subtle effect. The uniform approximation is obtained by applying a mapping

$$t^2 = \chi_1(\alpha, \theta) - \chi(\alpha_s, \theta),$$

and approximating the integral in the t plane. Details can be found in Thompson (2003) and (2006). In particular, there are two singularities in the t plane corresponding to $\alpha = \alpha_0$. This is because $\chi_1(\alpha, \theta)$ is a multi-valued function, and the specular pole exists on *all* sheets, including those where $\chi_1(\alpha_0; \theta) = -\mathrm{i}k(\Theta)\cos(\Theta + \theta)$. If we introduce

$$\psi_m = \mathrm{i}\big[k(\beta)\cos(\beta - \theta) - k(\Theta)\cos(\Theta + (-1)^m\theta)\big], \quad m \in \{1, 2\}, \qquad (3.15)$$

then the correction term, which is added to (3.10) to yield the uniform approximation may be expressed as

$$
W^{\mathrm{cor}} = -\frac{f(\alpha_0)}{2\phi^0\lambda_1^0} e^{i\frac{\hat{r}}{N}k(\beta)\cos(\beta-\theta)} \left\{ \mathrm{w}\left[e^{i\pi/4}\sqrt{\frac{\hat{r}}{N}|\psi_1|}\,\mathrm{sgn}(\beta-\Theta)\right] - \frac{e^{i\pi/4}\,\mathrm{sgn}(\beta-\Theta)}{\sqrt{\frac{\pi\hat{r}}{N}|\psi_1|}} \right.
$$
$$
\left. \pm\, \mathrm{w}\left[e^{i\pi/4}\sqrt{\frac{\hat{r}}{N}|\psi_2|}\,\mathrm{sgn}(2\pi-\beta-\Theta)\right] \mp \frac{e^{i\pi/4}\,\mathrm{sgn}(2\pi-\beta-\Theta)}{\sqrt{\frac{\pi\hat{r}}{N}|\psi_2|}} \right\}, \quad (3.16)
$$

where the upper and lower signs are to be taken in the symmetric and antisymmetric cases, respectively, and $\mathrm{w}(z)$ is the scaled complex error function (Abramowitz and Stegun, 1965), i.e. $\mathrm{w}(z) = e^{-z^2}\mathrm{erfc}(-iz)$. The function $\mathrm{sgn}(2\pi-\beta-\Theta)$ has been included so as to show that this has the correct symmetry properties (note that $2\pi - \theta(\beta) = \theta(2\pi-\beta)$); it is only actually necessary to consider $\beta \in [0,\pi]$ in order to construct the solution. The process of obtaining this result is fairly involved but is similar to the derivation given by Bleistein & Handelsmann (1986), taking into account the fact that the exponent function is multivalued (Thompson, 2006). It is straightforward to demonstrate that (3.16) is correct. Two properties of the scaled complex error function are required: the identity $\mathrm{w}(z) = 2e^{-z^2} - \mathrm{w}(-z)$, and the asymptotic approximation $\mathrm{w}(z) \sim i/(z\sqrt{\pi})$, which is valid for large $|z|$ and $-\pi/4 < \arg(z) < 5\pi/4$. Together these show that outside the Fresnel regions the correction term makes no contribution to the leading order behaviour of the diffracted field except for a plane wave in the region where $\beta < \Theta$. When the symmetric and antisymmetric components are combined we find that this contribution eliminates the incident field in the shadow region, whereas for $\hat{y} < 0$ it represents the plane wave component of the reflected field (§3d). Furthermore, the uniform approximation

$$
W^{\mathrm{uni}} = W^{\mathrm{sad}} + W^{\mathrm{cor}} \tag{3.17}
$$

is regular in θ. The simplest way to demonstrate this is to use the fact that $\psi_1 = \chi_1(\alpha_s,\theta) - \chi_1(\alpha_0,\theta)$, and then Taylor expand $\chi_1(\alpha,\theta)$ about $\alpha = \alpha_s$. This yields

$$
\sqrt{|\psi_1|} = |\alpha_s - \alpha_0|\sqrt{|\chi_1''(\alpha_s,\theta)|(\tfrac{1}{2} + O(\alpha_s - \alpha_0))},
$$

and the result then follows immediately since $\mathrm{sgn}(\beta - \Theta) = \mathrm{sgn}(\alpha_s - \alpha_0)$.

The uniform approximation (3.17) has the special property that it remains valid when $\theta = \pi$, and $\Theta \approx \pi$, so that the two Fresnel regions overlap, and the observer is positioned inside this region. To demonstrate this, take $\hat{y} = 0$ and $x < 0$ in equation (2.20), and deform the contour of integration into the upper half plane. Obviously, the antisymmetric component gives no contribution. Also, the dominant contribution comes from the branch point $\alpha = 1$, which the ratio $f_2^S/(\phi\lambda_1)$ does not possess. Taking the uniform (in Θ) approximation to the resulting branch line integral yields

$$
W(x < 0, 0) \sim \frac{D_1}{\sqrt{HD_y}}\frac{e^{3i\pi/8}e^{i|\hat{x}|/N}}{2^{3/4}\sqrt{\pi|x|\psi_1}}(-k(\Theta)\cos\Theta - i)^{1/2}K_-^0 K_+(1)L_1^0
$$
$$
- \frac{K^0\lambda_2^0(L_1^0)^2}{2\phi^0}e^{i|x|}\left[\mathrm{w}\left(e^{i\pi/4}\sqrt{|x|\psi_1}\right) - \frac{e^{i\pi/4}}{\sqrt{\pi|x|\psi_1}}\right],
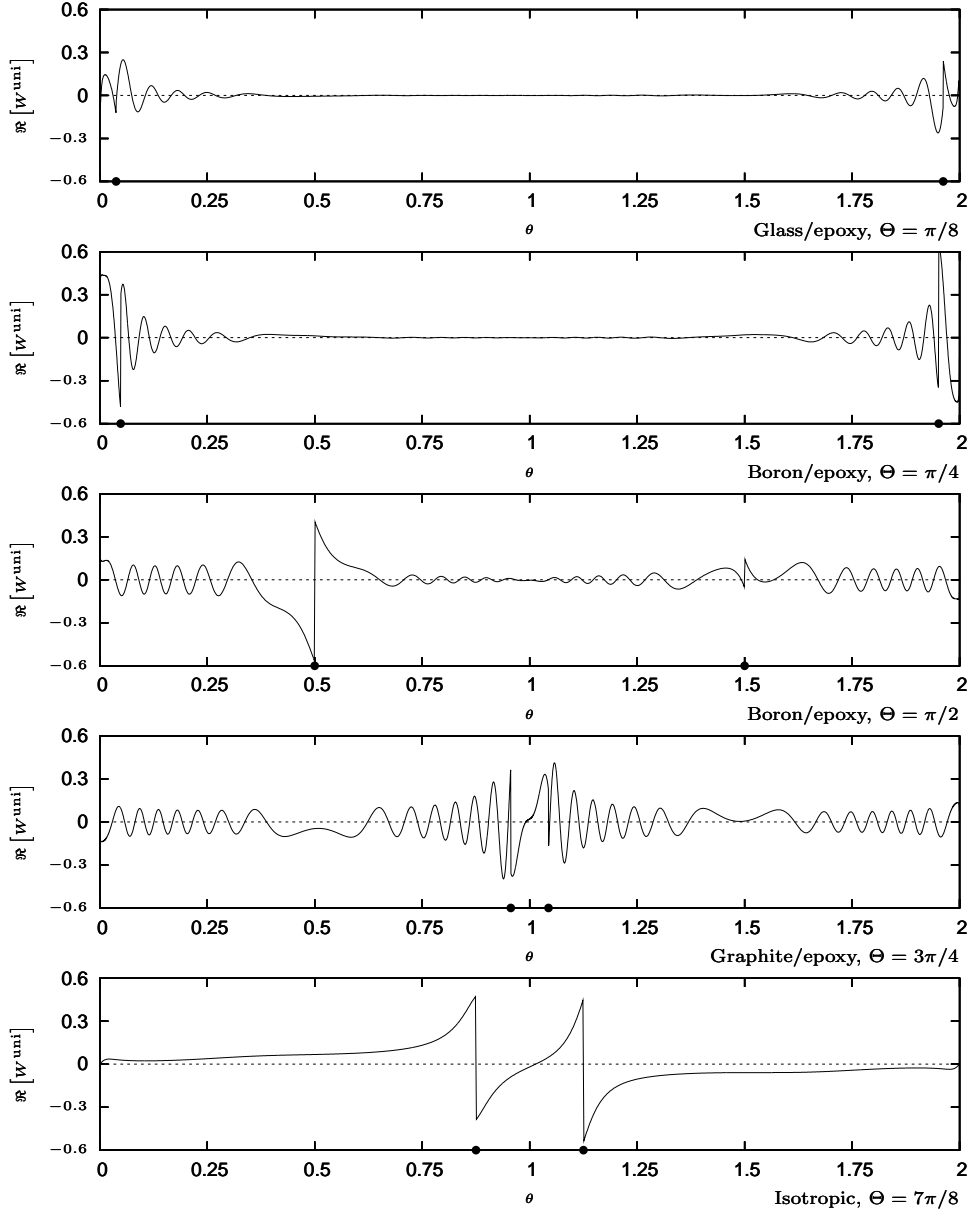$$

Figure 8. Real part of the diffracted field, using the uniform approximation, for the materials in table 1, with non-dimensional radial distance $\hat{r} = 100$. The shadow and reflection boundaries are denoted by circular marks on the horizontal axes. Plane wave terms are not included.

where ψ_1 can be evaluated to yield $\psi_1 = 1 + k(\Theta)\cos(\Theta)$, and the argument of the fractional power lies in the interval $(-\pi/2, \pi/2]$. See Thompson (2003) for details. Exactly the same result can be obtained by evaluating the uniform approximation with $\theta = \pi$; the first term comes from W^{sad}, and the second from W^{cor}.

Figure 8 shows the real part of the diffracted field, with plane wave terms omitted and $\hat{r} = 100$, for various materials (table 1) and angles of incidence. The imaginary part exhibits a qualitatively similar behaviour, and is not shown. The oscillation as θ is varied, and the expansion (or contraction) of the shadow and reflection regions due to orthotropy are clearly visible. Also, note the cessation of oscillations in regions where $\cos\theta \approx 0$. The discontinuities due to omission of specular contributions are most clearly distinguishable when the frequency of oscillation is low. The field is stronger inside the shadow and reflection regions than in the lit region; this is particularly visible when $\theta = \frac{\pi}{2}$. For the smaller values of θ, the field is near zero in a large portion of the lit region. In all cases, the antisymmetric contribution is dominant; this is particularly noticeable outside the Fresnel regions. Finally, note that taking $\Theta = \frac{3\pi}{4}$ for graphite/epoxy causes the Fresnel regions to overlap, however the uniform approximation remains accurate here, and in particular, the plot is continuous at $\theta = \pi$.

(d) The reflected field

For $y < 0$, the residue from the specular pole gives the reflected field, which takes the form

$$W^{\mathrm{ref}} = c \exp\left\{ \mathrm{i}\frac{k(\Theta)}{N}[\hat{x}\cos\Theta - \hat{y}\sin\Theta] \right\}$$
$$- \frac{L_1^0}{L_2^0}(1+c)\exp\left\{ \frac{k(\Theta)}{N}\left[\mathrm{i}\hat{x}\cos\Theta + \hat{y}\sqrt{2\frac{H}{D_y}\cos^2\Theta + \sin^2\Theta}\right] \right\}, \quad (3.18)$$

wherein c is the reflection coefficient defined above (2.39). Here, the first term represents a plane wave whose phase velocity travels at angle of inclination $-\Theta$ to the y axis. This is the principal part of the reflected field. Note that $|c| = 1$, since all of the terms in (2.39) are real, except λ_1, which is pure imaginary. The second term is an evanescent mode, which propagates along the lower face of the crack, and decays exponentially as $|y|$ increases. It is absent from the far field approximation discussed in §3c due to the omission of terms with exponent χ_2, however it is a significant component of the field on the lower face of the crack, and plays a role in the satisfaction of the boundary conditions. The argument of c for the materials given in table 1 is shown in figure 9. In each case, we have $\arg[c] \in [0, \pi]$ for all Θ. This is evident from equation (2.39), since the numerator and denominator reside in the lower right and lower left quadrants of the complex plane respectively. As $\sin\Theta \to 0$, the incident field approaches symmetry about the crack, and $\arg[c] \to \pi$. Again this can be deduced from equation (2.39). In this limit, $c \to -1$, hence the evanescent wave disappears, and the contribution from the specular pole becomes symmetric about $y = 0$. For $\Theta = \frac{\pi}{2}$, in which case $\alpha_0 = 0$, it is easy to show from equations (2.29), (2.30) and (2.25) that $c = \mathrm{i}$, regardless of material parameters. The modulus of the evanescent wave is also shown in figure 9. From equation (2.39), it is not difficult to show that

$$\left| \frac{L_1^0}{L_2^0}(1+c) \right| = 2\left[\frac{(L_1^2\lambda_2 - L_2^2|\lambda_1|)^2}{L_1^2L_2^2|\lambda_1|^2} + 2\frac{\lambda_2}{|\lambda_1|} \right]_{\alpha=\alpha_0}^{-1/2}.$$

For $\alpha \in [-1, 1]$, we have $|\lambda_2| \geq |\lambda_1|$, and $|L_2| \geq |L_1|$, with equality holding in both cases when $\alpha = 0$. Thus, for any material, the magnitude of this component is at a
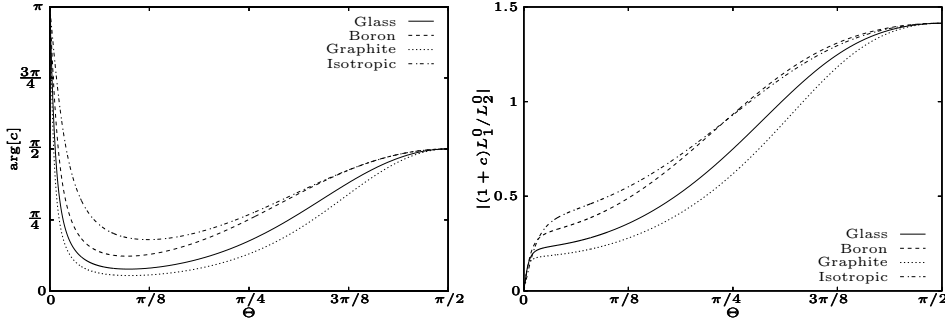
Figure 9. Left: The argument of the reflection coefficient c. Right: The amplitude of the
evanescent wave.

maximum ($\sqrt{2}$) when $\Theta = \frac{\pi}{2}$, which is to be expected, since it is an effect due to
asymmetry.

(e) The diffracted edge waves

Close to the crack faces, the residue contribution from the pole $\alpha = -\alpha_e$ (2.34)
becomes significant; this is a diffracted edge wave, with the form

$$W^{\text{edge}} = e_1(\Theta)e^{-r\chi_1(-\alpha_e,\theta)} + e_2(\Theta)e^{-r\chi_2(-\alpha_e,\theta)}. \tag{3.19}$$

This propagates along both faces of the crack, and decays exponentially as $|y|$
increases. The edge wave generates zero bending moment and Kirchhoff shear on
the edge; from these conditions it can be determined up to a single constant, see
Norris (1994). Analogously, from equations (2.36–2.37), we observe that

$$e_2^S = -e_1^S(\lambda_1^e L_2^e)/(\lambda_2^e L_1^e), \qquad\qquad e_2^A = -e_1^A(L_1^e/L_2^e), \tag{3.20}$$

where we have introduced the superscript 'e' to refer to evaluation at the point
$\alpha = \alpha_e$ (λ_m and L_m are even functions of α). These relationships are, in fact,
identical in view of the fact that $\alpha = -\alpha_e$ is a pole of the function K, and therefore

$$\lambda_2(\alpha_e)L_1^2(\alpha_e) = \lambda_1(\alpha_e)L_2^2(\alpha_e).$$

Thus, in Cartesian co-ordinates, the edge wave is given by

$$W^{\text{edge}} = [e_1^S + \text{sgn}(\hat{y})e_1^A]\left[e^{-\lambda_1^e|\hat{y}|/N} - (L_1^e/L_2^e)e^{-\lambda_2^e|\hat{y}|/N}\right]e^{i\alpha_e\hat{x}/N}. \tag{3.21}$$

Now, $\alpha_e > 1$, and the restriction (2.7) ensures that $\alpha_e < \alpha_\phi$ in cases where $D_x D_y >
H^2$. Hence, both λ_1^e and λ_2^e are pure real and positive, the latter being greater than
the former. Thus, although the edge wave propagates without loss along the faces
of the crack, it decays exponentially as $|\hat{y}|$ increases, the second term decreasing
more rapidly than the first. Values of the various Θ invariant coefficients are given
to six decimal places in table 2. Note that we have $L_2^e > L_1^e$ for all materials, since
$L_2^e - L_1^e = 2\phi^e > 0$, therefore the second term in (3.21) possesses a smaller amplitude
coefficient than the first. The non-dimensional wavelength N/α_e is also shown; note
that this is greater in the more rigid materials. Hence, as in the case of plane waves,

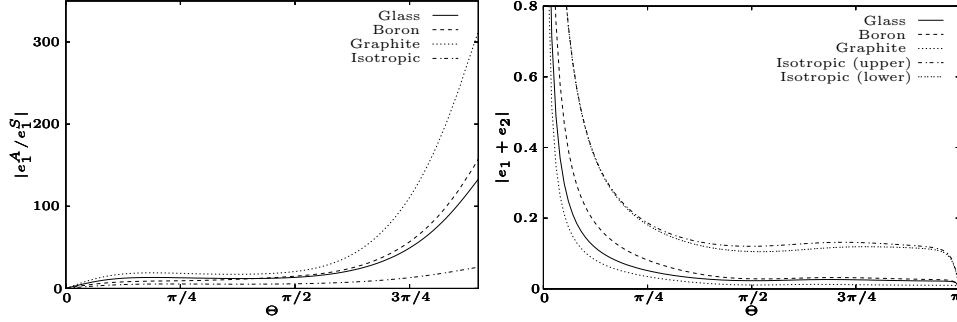|	α_e	λ_1^e	λ_2^e	$-L_1^e/L_2^e$	N/α_e
Glass/epoxy	1.000061	0.021333	1.579008	0.116233	1.579003
Boron/epoxy	1.000041	0.032954	1.289147	0.159883	2.236221
Graphite/epoxy	1.000011	0.015340	1.825344	0.091672	2.387079
Isotropic	1.001956	0.062579	1.415597	0.210254	0.998048

Table 2. *Values of the Θ independent edge wave coefficients.*

Figure 10. Left: Relative strengths of the edge wave's symmetric and antisymmetric components. Both vanish as $\Theta \to \pi$, hence the horizontal axis is restricted to $\Theta \in [0, \frac{9\pi}{10}]$. Right: Overall strength of the edge wave on the crack faces. The difference in magnitude between the waves on the upper and lower faces is visible only for the isotropic material.

the phase velocity of edge waves under an equal frequency of excitation increases with the rigidity of the conducting medium. The final coefficient e_1 is determined by the incident wave; from equation (2.20), we find that

$$e_1^S = \frac{K_-^0 \gamma_-^0 L_1^0 \lambda_2^e L_1^e}{K_+^e (\alpha_e + \alpha_0)} \mathcal{L}, \qquad e_1^A = -\frac{K_-^0 \lambda_1^0 L_2^0 \gamma_+^e L_2^e}{K_+^e (\alpha_e + \alpha_0)} \mathcal{L}, \qquad (3.22)$$

where the limit $\mathcal{L}$ is given by

$$\mathcal{L} = \lim_{\alpha \to \alpha_e} (\alpha_e - \alpha) K(\alpha)/(2\phi\gamma_+).$$

Note that we have exploited the fact that $K_+(\alpha) = K_-(-\alpha)$ (and similarly for γ) so as to express e_1 in terms of functions evaluated at $\alpha = \alpha_e$ and not $\alpha = -\alpha_e$. Making use of equation (2.33), and expanding the denominator, this reduces to

$$\mathcal{L} = \frac{D_x^2}{(\lambda_1^e - \lambda_2^e)\gamma_+^e} \lim_{\alpha \to \alpha_e} \frac{\alpha_e - \alpha}{(D_x D_y - D_1^2)\alpha^4 + 4D_y D_{xy} \alpha^2 \gamma - D_x D_y},$$

which is determined via L'Hopital's rule. We find that

$$\mathcal{L} = \frac{D_x^2}{\lambda_2^e - \lambda_1^e} \frac{\gamma_-^e}{4\alpha_e} \left[(D_x D_y - D_1^2)\alpha_e^2 \gamma^e + 4D_x D_{xy}(\alpha_e^4 - \tfrac{1}{2}) \right]^{-1}.$$

Figure 10 shows plots of $\left| e_1^A / e_1^S \right|$ against Θ, thus illustrating the relative strength of the symmetric and antisymmetric components of the edge wave. In each case, the

antisymmetric contribution is generally much larger. As $\Theta \to 0$, the wave becomes symmetric, as we should expect, and as $\Theta \to \pi$, both contributions disappear, therefore the domain of the incidence angle is restricted to $[0, \frac{9\pi}{10}]$ here. Note that e_1^A is symmetric about $\Theta = \frac{\pi}{2}$; this is evident from equation (3.22). Figure 10 also shows plots of $|e_1 + e_2|$ against Θ, thereby illustrating the overall strength of the edge wave on the crack faces. In each case, the wave gains strength as Θ is decreased, due to the factor $\alpha_e + \alpha_0$ in the denominator of e_1 (3.22). Typically, the wave is marginally stronger on the upper side of the crack, however this is visible only in the isotropic case, which has a greater edge wave amplitude than the other materials. Note that the difference in amplitude on the upper and lower faces remains small, even as $\Theta \to 0$, when $|e_1| \approx |e_2|$. In this limit, we have $\alpha_0 = -1$, and, since $\alpha_e \approx 1$ it is not difficult to show from equation (3.22) that $\arg[e_1^S/e_1^A] \to \frac{\pi}{2}$, which explains the effect.

4. Conclusions

Despite the complexity of the diffraction integrals involved, the scattered field can be approximated by a relatively straightforward asymptotic analysis. Many of the effects observed by Norris & Wang (1994) in the isotropic case persist under orthotropy; in particular the diffracted field is strongly, though not entirely, antisymmetric. In addition, a number of characteristics exhibited by the scattered field are unique to anisotropic cases. Central to these are the wavelength and group velocity of the incident field. The former tends to increase with the rigidity of the material, leading to stronger decaying modes and higher wavespeeds under equal frequency of excitation. The orientation of group velocity, that is the direction of energy propagation, determines the size of the shadow and reflection regions. In general, there is no reciprocity in the scattered field. The diffracted edge wave, which propagates along the crack faces, and is strongest for small angles of incidence, also possesses greater wavelength in more rigid media.

References

Abramowitz, M. and Stegun, I. 1965 *Handbook of Mathematical Functions.* Dover.

Bleistein, N. and Handelsmann, R. A. 1986 *Asymptotic Expansions of Integrals.* Dover.

Crighton, D. G., Dowling, A. P., Ffowcs Williams, J. E., Heckl, M., and Leppington, F. G. 1992 *Modern Methods in Analytical Acoustics.* Springer-Verlag.

Fu, Y. B. 2003 Existence and uniqueness of edge waves in a generally anisotropic elastic plate. *Quarterly Journal of Mechanics and Applied Mathematics* **56** (4), 605–616.

Jeffreys, H. and Jeffreys, B. 1956 *Methods of Mathematical Physics.* Cambridge University Press.

Jones, R. M. 1975 *Mechanics of Composite Materials.* Hemisphere.

Kollár, L. P. and Springer, G. S. 2003 *Mechanics of Composite Structures.* Cambridge University Press

Konenkov, Y. K. 1960 A Rayleigh-type flexural wave, *Soviet Physics Acoustics* **6**, 122–123.

Lighthill, J. 2002 *Waves in Fluids.* Cambridge University Press.

Norris, A. N. 1994 Flexural edge waves. *Journal of Sound and Vibration* **171**(4), 571–573.

Norris, A. N. and Wang, Z. 1994 Bending-Wave Diffraction from Strips and Cracks on Thin Plates. *Quarterly Journal of Mechanics and Applied Mathematics* **47**(4), 607–627.

Timoshenko, S. and Woinowsky-Krieger, S. 1959 *Theory of Plates and Shells.* McGraw-Hill.

Thompson, I. 2003 *Flexural Wave Diffraction by Cracks in Orthotropic Thin Elastic Plates.* PhD thesis, University of Manchester.

Thompson, I. 2006 An improved uniform approximation for diffraction integrals. *Proceedings of the Royal Society A* **462** (2069), 1341–1353.

Thompson, I. and Abrahams, I. D. 2005 Diffraction of flexural waves by cracks in orthotropic thin elastic plates. Part I: formal solution. *Proceedings of the Royal Society A* **461** (2063), 3413–3436.

Thompson, I., Abrahams, I. D. and Norris A. N. 2002 On the existence of flexural edge waves on thin orthotropic plates. *Journal of the Acoustical Society of America* **112** (5), 1756–1765.

Zakharov, D. D. 2002 Konenkov's waves in anisotropic layered plates. *Acoustical Physics* **48** (2), 171–175.

Figure captions

Figure 1: The thin elastic plate with flexural waves incident at angle Θ upon a semi-infinite crack along $x > 0$, $y = 0$.

Figure 2: Polar plots of the normalised wavenumber $|\hat{\mathbf{v}}|$ against the direction of phase velocity Θ, for several materials (see table 1). These are equivalent to slowness surfaces with $\omega = 1$.

Figure 3: Steepest descent paths in the isotropic case. For $\theta \geq \pi/4$ the contour has the correct orientation with respect to all of the branch points, whereas if $\theta < \pi/4$, it must be diverted as shown. The contribution from the branch point is exponentially small.

Figure 4: Left: the deformed integration paths for a boron/epoxy composite plate with observation angles $\theta = \frac{\pi}{2}$, $\theta = \frac{\pi}{4}$ and $\theta = \frac{\pi}{100}$. In the case $\theta = \frac{\pi}{100}$, the saddle is very close to the branch point $\alpha = -1$. Right: the smaller real part $\Re_{\min}$ of the two exponent functions χ_1, χ_2 evaluated on the deformed integration path. Positive (negative) arc length refers to the branch of the path to the right (left) of the saddle. Note that discontinuities in the gradient of $\Re_{\min}$ can occur at points where the integration path is diverted, and also where $\Re[\chi_1] = \Re[\chi_2]$.

Figure 5: Left: Direction of propagation of group velocity, Ψ as a function of incidence angle Θ. Right: Location of the saddle point α_s as a function of observation angle θ.

Figure 6: Variation of the exponential term in the saddle contribution with observation angle θ.

Figure 7: Polar plots of the modulus of $\hat{D}(\theta)$, the non-specular diffraction coefficient.

Figure 8: Real part of the diffracted field, using the uniform approximation, for the materials in table 1, with non-dimensional radial distance $\hat{r} = 100$. The shadow and reflection boundaries are denoted by circular marks on the horizontal axes. Plane wave terms are not included.